ABSTRACT

PHILLIPS, BRITTANY NICOLE Hygroscopicity- and size-resolved measurements of submicron aerosol on the East Coast of the United States. (Under the direction of Nicholas Meskhidze and Markus Petters).

Aerosols, particles suspended in the air, are known to influence the climate by scattering light (direct radiative effect) and by changing cloud properties (indirect radiative effects). Presented in this study are aerosol hygroscopicity and size-resolved data collected during a field deployment on the East Coast of the United States. Air mass back trajectories show that the aerosol sampled at the coast were originated over the continent (continental) as well as over the Atlantic Ocean (marine). The hygroscopicity and size-resolved measurements compared for the different air masses show that air masses of marine origin were heavily influenced by the continental outflow. Aerosol number size distributions showed Aitken modes ranging from 49.1±1.7 nm to 66.9±0.8 nm and accumulation modes ranging from 142.8±1.1 nm to 155.0±2.8 nm. Hygroscopicity distributions for 96 nm, 188 nm, and 284 nm dry-sized particles showed the mode hygroscopicity parameter (κ) ranged from 0.20±0.01 to 0.54±0.03, suggesting the presence of anthropogenic aerosols. A recently developed method was used for decomposing hygroscopicity distributions into three distinct hygroscopicity classes based on the ambient aerosol hygroscopic properties relative to the hygroscopic properties of a reference compound. The method shows that at the East Coast of the US, sub-micron aerosols are mostly comprised of ammonium sulfate (64% to 85%), with small a contribution from carbonaceous particles and sea-salt (up to 38% and 8%, respectively). The results presented in this study will help constraining climate forcing by anthropogenic aerosols.

Hygroscopicity- and Size-Resolved Measurements of Submicron Aerosol on the East Coast of the United States

by
Brittany Nicole Phillips

A thesis submitted to the Graduate Faculty of
North Carolina State University
in partial fulfillment of the
requirements for the degree of
Master of Science

Marine, Earth, and Atmospheric Sciences

Raleigh, North Carolina

2017

APPROVED BY:

_____	_____
Dr. Nicholas Meskhidze	Dr. Markus Petters
Committee Co-Chair	Committee Co-Chair

_____
Dr. Andrew Grieshop

DEDICATION

I want to thank my fiancé, Taylor for his continuous support and love throughout the past three years. I would not have completed this without you.

BIOGRAPHY

Brittany was born in Greer, South Carolina on December 27, 1991 to Christopher and Kimberly Pike. Brittany graduated from Greer High School in Greer, SC in May 2010. A first-generation college student, Brittany attended Western Carolina University and received her B.S. in Electrical Engineering in May 2014. Brittany attended graduate school at North Carolina State University in Raleigh, NC and studied marine aerosol under the advisement of Dr. Nicholas Meskhidze.

ACKNOWLEDGMENTS

This work was funded by NSF Grant No. AGS-1249273. We thank Dr. Jeff Waters and the rest of the FRF staff for allowing us to use the U.S. Army Corps of Engineers' field research facility at Duck, NC. The authors gratefully acknowledge the NOAA Air Resources Laboratory (ARL) for the provision of the HYSPLIT transport and dispersion model and/or READY website (http://www.ready.noaa.gov) used in this publication.

Additionally, I would like to thank Kyle and Tim for always being willing to help out with any questions regarding code or things in the lab.

TABLE OF CONTENTS

LIST OF TABLES

LIST OF FIGURES

CHAPTER 1

1.1 INTRODUCTION

Atmospheric aerosols originate from two general sources: anthropogenic and natural. Anthropogenic sources include industrial processes, land use change, biomass burning, transportation, and agricultural operations. Natural sources include volcanoes, dust storms, oceans, and terrestrial plants. Aerosols are important due to their influence on both radiative effects and radiative forcing. The radiative effects of aerosols describe how they interact with incoming solar radiation, either cooling or warming, depending on the aerosol constituent. The radiative effects of aerosols occur both directly and indirectly. Directly, aerosols scatter and absorb solar radiation. Indirectly, aerosols interact with clouds to influence their albedo and lifetime. The radiative forcing of aerosols describes how anthropogenic aerosols have changed the net incoming solar radiation since pre-industrial times. Although anthropogenic emissions are suspected to have influenced climate through these effects, the magnitude is generally uncertain. A significant source of this uncertainty comes from the indirect forcing of anthropogenic aerosols and has been attributed to the uncertainty in the background concentration of naturally produced aerosols. [*Lohmann et al.*, 2000; *Hoose et al.*, 2009; *Wang and Penner*, 2009; *Gantt et al.*, 2012; *Carslaw et al.*, 2013].

In an effort to constrain the uncertainty in anthropogenic aerosol forcing attributed to the uncertainties in the natural background aerosol, recent authors [*Ovadnevaite et al.*, 2014; *Modini et al.*, 2015, *Royalty et al.*, submitted] seek to quantify the contribution of primary ocean-sourced aerosol, arguably an important constituent to the marine boundary layer (MBL) aerosol number budget. In general, results from these studies suggest that the

contribution of primary ocean-sourced aerosol to the total aerosol number budget for the MBL may be lower than previously estimated [*de Leeuw et al.,* 2011]. A potential consequence from this suggestion is that continental outflow may have a larger role in regulating the MBL aerosol number budget and atmospheric chemistry. Continental outflow is the movement of continentally-derived pollution from over the continent over the coasts and eventually the ocean. Thus, characterization of atmospheric chemistry, meteorology, cloud physics, and climate at coastal sites (i.e. processes controlling outflow) is important for understanding and observing the interactions between marine air masses and continental outflow [*Wood et al.*, 2017].

In addition to the importance in constraining the uncertainty in climate forcing, better understanding of air quality at coastal sites is important as a large percentage of the Earth's population live near coastal regions. Specifically, surf zone production can influence local air quality. For example, sea-spray aerosol could possibly suppress regional surface-level ozone concentrations [*Sarwar et al.*, 2015], promote HNO_3 deposition [*Vignati et al.*, 2001; *Gantt et al.*, 2015] as well as lead to the aerosolization of toxins associated with hazardous algal blooms [*Backer et al.*, 2005; *Cheng et al.*, 2005]. Generally speaking, model representation of aerosols along coastlines is especially difficult because of i) the presence of several different sources: aerosols of marine origin become mixed with aerosols originating over land, from natural sources as well as from anthropogenic sources such as urban and industrial activities [*Li et al.*, 2005], ii) fast temporal and spatial changes in concentration, size distribution, and chemical composition [*Xia and Gao*, 2010], and iii) atmospheric models dealing with coastlines have to consider the sudden change in numerous surface variables:

roughness, temperature, bathymetry, etc. [*Vignati et al.*, 2001; *Gantt et al.*, 2015] which are important for accurate model representation of aerosols. Coastal aerosol and meteorological measurements are essential as they provide information to improve model representation.

Here, back trajectories, aerosol size, and aerosol hygroscopicity dynamics are reported from a field deployment at the US Army Corps of Engineers Field Research Facility (FRF) in Duck, North Carolina, from 29 April 2016 to 16 May 2016. Aerosol size and hygroscopicity measurements were made with a scanning mobility particle sizer (SMPS) [*Wang and Flagan*, 1990] and hygroscopicity tandem differential mobility analyzer (HTDMA) [*Rader and McMurry*, 1986], respectively. Hygroscopic properties have been represented by a single parameter, the hygroscopicity parameter, or κ. [*Petters and Kreidenweis*, 2007]. The range of κ values in the atmosphere is $0 < \kappa < 1.2$, with higher values ($\kappa > 0.5$) indicating a more hygroscopic constituent (e.g., inorganic salts), lower values ($\kappa < 0.5$) indicating a less hygroscopic constituent (e.g., organic species), and zero indicating non-hygroscopic constituents. HTDMA measurements are of particular interest as they provide hygroscopicity growth distributions which show dominating hygroscopicities within an air mass. However, if an aerosol external mixture is highly complex or strongly dominated by a single composition, minor signals in the hygroscopicity distribution can be masked. As these minor components may have implications towards local air quality and continental outflow properties, quantifying their relative contributions to the coastal aerosol budget is important. As such, the kernel fractionation method, developed by *Royalty et al.* [submitted], was applied to hygroscopicity growth distributions which decomposed and quantified hygroscopicity distributions into three different classes (sodium-containing,

sulfate-like, and carbon-containing) based on the hygroscopic properties of a known, aerosolized reference compound. Results associated with the kernel fractionation method, aerosol size distributions, the aerosol hygroscopicity growth distributions, and back trajectories are discussed below.

1.2 METHODS

1.2.1 Research Site

The research was performed at the US Army Corps of Engineers' Field Research Facility in Duck, North Carolina [*Birkemeier et al*. 1985]. Measurements were obtained between 29 April and 16 May 2016. Instruments were located inside an air-conditioned trailer at the end of a 560 m long pier (36°10'54.6" °N, 75°45'5.2" °W) that protrudes perpendicular to the shoreline into the Atlantic Ocean. The trailer was located 14.3 m from the edge of the pier. Figure 1.1 shows a schematic diagram of the pier and location of the instruments. An ultrasonic anemometer (RM Young model 81000) measured the three-dimensional wind speed and direction. The anemometer was mounted on a mast at the far end of the pier, approximately 15.4 m above the ocean's surface. Wind speed and direction data were acquired at 20 Hz frequency. Two sample inlets were installed to measure ambient aerosol at different heights: one 0.5 m above the sonic anemometer and one 12.5 m below the sonic anemometer. These inlets are referred to as 'upper' and 'lower' line, respectively. The measurements derived from the upper and lower lines were combined for analysis here as the concentration and size distributions did not show a significant difference between the two. A mix of conductive silicone and stainless steel tubing (4.4 mm and 5.8 mm inner diameter, respectively) was used to route sample air from the inlets to the inside of the instrument

trailer. Inside the trailer, the upper or lower sample flow line or aerosol from an atomizer was directed to the aerosol instrumentation using a computer-controlled three-way solenoid-valve board. The instrumentation included three condensation particle counters (CPC), a scanning mobility particle sizer (SMPS), and a hygroscopicity tandem differential mobility analyzer (HTDMA) shown in Figure 1.1.

1.2.2 Size Distribution Measurement

Figure 1.1 shows that sample flow exiting the valve board was split between CPC-1 (TSI Inc. 3022A), to measure total particle number concentration with diameter $D > 5$ nm, and the SMPS and HTDMA instruments. Before entering the sizing instruments particles were charge equilibrated using an X-Ray neutralizer (TSI Inc. Model 3088) and dried to relative humidity (RH) = 6% ± 2.0% using a Nafion membrane drier. RH was measured using a Rotronic Hygroclip HC2 sensor. The SMPS consisted of a long column differential mobility analyzer (DMA-1, TSI Inc. 3081) that was operated with a sheath-to-sample flow ratio of 5:0.6 L min^{-1}. Particles were counted using CPC-2 (TSI Inc. 3787). The SMPS was configured to perform an exponential voltage scan from 10 kV to 10 V over a 6 min interval, corresponding to a mobility diameter range from 554 to 10 nm. Raw 1 Hz CPC counts were inverted to derive the size distribution as described elsewhere [*Nguyen et al.*, 2014]. Briefly, the inversion includes mapping for the time varying electric field to mobility diameter [*Wang and Flagan*, 1990] and inversion from counts to total concentration while accounting for multiply charged particles [*Petters et al.*, 2009]. Particle losses in the Nafion dryer were characterized experimentally and an appropriate loss correction parameterization was applied to the inversion. The resulting data were binned into 32 geometrically spaced bins from 10 to

554 nm diameters and normalized by the $\log_{10}$ of the bin width (i.e., expressed as $dN/d\log_{10}D_P$).

1.2.3 HTDMA Measurement

The HTDMA setup is also shown in Figure 1.1. The HTDMA comprised DMA-2 (TSI Inc. 3081) to create monodispersed particles, a high-flow DMA column (DMA-3) [*Stolzenburg et al.*, 1998] to scan the humidified size distribution, and CPC-3 (TSI Inc. 3771) to count particles. Due to instrument failure, CPC-3 was replaced with CPC-1 (TSI Inc. 3022A) in the middle of the deployment and total particle concentration measurements were discontinued. As CPC-3 operated at 0.3 L min^{-1}, 0.7 L min^{-1} particle-free make-up flow was added to maintain a consistent sheath-to-sample flow ratio in DMA-2 and DMA-3 throughout the deployment. The humidification and thermal stabilization of the high-flow DMA-3 was as described previously [*Suda and Petters*, 2013; *Dawson et al.*, 2016]. Relative humidity was monitored in the sheath and sample flow of both DMA-2 and DMA-3 using the HC2.

The HTDMA setup measured the humidified size distribution of the size-selected particles. The aerosol was dry size-selected by electric mobility with DMA-2 that was operated at a nominal sheath-to-sample flow ratio of 5:1 L min^{-1}. The dry size-selected aerosol was humidified to ~80% RH in the humidification system that consisted of aerosol passing through a Nafion membrane immersed in a temperature controlled water bath. DMA-3, operating at a nominal sheath-to-sample flow ratio of 9:1 L min^{-1}, measured the humidified size distribution. The voltage scan strategy was similar to that of the SMPS system. The main difference was selection of a narrower voltage range that was dictated by the selected dry

diameter. The nominal dry size was confirmed using 'dry-dry' scans that were achieved by manually bypassing the humidification systems. Dry-dry scans were performed at the beginning, middle, and end of the deployment. The measured dry diameters were 96, 188, and 284 nm and within 2-5% of the set nominal dry diameter. Figure A.1 and Table A.1 show the dry-dry scans and the percent difference between the set and measured dry diameters. These dry diameters were chosen to target the peak in the emission flux parameterizations [*de Leeuw et al.*, 2011]. Humidified size distribution scans lasted 2 min. The scan ranges were 60-250 nm, 120-500 nm, and 180-750 nm for the three selected dry diameters. Relative humidity was determined using calibration scans with ammonium sulfate aerosol. The observed humidified size of the ammonium sulfate was used to calculate the RH in the system at the time of the scan [*Suda and Petters*, 2013]. These calibration scans were performed for each dry diameter every hour. Figure 1.2 shows an example of the time series of valve and instrument operation for the one hour instrument duty cycle. This sequence kept repeating for the duration of the campaign. The order of operation was as follows, upper line, lower line, line 3, line 4, and calibration. Data from line 3 and line 4 are not discussed in the manuscript.

The aerosol growth factor (GF) was calculated from the ratio of humidified diameter (D) to dry diameter (D_d). The measured dry diameters from the dry-dry scans was used for all calculations. The raw 1 Hz CPC-3 (CPC-1 after 4 May) data was inverted to derive the humidified size distribution, and in turn, the growth factor distribution. The method is described in detail in *Royalty et al*. [submitted]. Briefly, the inversion maps voltage to size and applies a calibration that ensures that the integral over the entire growth factor

distribution is consistent with the integrated number concentration of the corresponding slice of the size distribution selected by DMA-1. The growth factor distributions are converted into hygroscopicity parameter (κ) distributions as described in *Petters and Kreidenweis* [2007]. Calculations use the GF and calibrated RH from the closest calibration scan in time. Resulting κ distributions were interpolated onto a 32 bin, geometrically-stepped κ grid and distributions are normalized by the bin width, i.e., represented as $dN/d\log_{10}\kappa$. The 4 additional bins at 0.01, 0.02, 0.07, and 0.09 are included to more accurately represent the distribution for non-hygroscopic particles. Concentration normalized κ frequency distributions are calculated by dividing the $dN/d\log_{10}\kappa$ by the integrated concentration from the distribution. All κ distributions were manually inspected and filtered for incomplete scans.

1.2.4 Particle Classification

Particles were further classified into classes with different chemical composition using the method of *Royalty et al*. [submitted]. Briefly, the method is based on the conversion of the ambient GF distribution to probability density function (PDF) by dividing the GF distribution by the integrated counts in the distribution. Numerical simulations, supported by the ambient data, suggest that for marine environments, the PDFs of different dominating particle chemical compositions have hygroscopicities such that these particles can be classified into three hygroscopicities classes: sodium-containing, sulfate-like, and carbon-containing [*Royalty et al*., submitted]. The data analyses carried out by *Royalty et al*. [submitted] show that the GF distribution of ammonium sulfate (used as a proxy for the sulfate-like aerosols) provides a good reference PDF kernel for quantifying sodium-

containing and carbon-containing aerosols. Thus, the hourly ammonium sulfate calibration GF distributions were converted into PDFs. Despite good separation, small overlaps between the tails of the PDF kernel functions residing within the respective classes were noticed. Due to such overlap between the PDF functions, small fractions of sulfate-containing particles can be misinterpreted as sodium- and carbon-containing. To reduce the effect of overlap between the PDF functions, we carried out extensive numerical simulations which were similar to those of *Royalty et al*. [submitted]. The simulations were designed to minimize the uncertainty in the predicted concentrations of the three classes for the conditions associated with the measurement site and the DMA transmission function. Summary of all the simulations is provided as supporting information Table A.2. Based on these simulations, we found that for given RH conditions, one can derive the upper-threshold (4%) and the lower-threshold (1%) of the integrated value of ammonium sulfate GF distribution PDF. The ammonium sulfate PDF is then compared to the ambient PDF. Particles in the ambient distribution that reside to the right (in the top 4%) of the ammonium sulfate GF distribution PDF are defined as more hygroscopic than ammonium sulfate and likely contain ocean-derived sodium (i.e., sea spray), while the particles that reside to the left (in the bottom 1%) of the ammonium sulfate GF distribution PDF are less hygroscopic than ammonium sulfate and defined to contain carbon. When subtracted from the measured ambient GF distribution, the area above the threshold value can be used to estimate the concentration of sodium-containing aerosol, while the area below the threshold value can be used to estimate the concentration of carbon-containing aerosol. The uncertainty of the particle classification method was tested by carrying out simulations with prescribed variable number

concentrations and chemical compositions for three different classes of aerosols. The simulation results summarized in Table A.2 show that for particles with a hygroscopicity similar to that of artificial seawater at RH 80%, the uncertainty in the reported concentration of the sodium-containing class is within ±50%, but can underestimate by as much as 100% when particles contain 70% organics. While this technique leads to satisfactory separation of the three classes, it could also yield negative values. This occurs when the fraction of particles, prior to subtraction, falling within sodium- and carbon-containing classes for a given ambient GF distribution is less than 4% and 1%, respectively. Thus, the derived particle concentrations in both the sodium- and carbon-containing classes should be interpreted as a lower limit to what might actually be present in the atmosphere.

1.2.5 Data Acquisition

Three computers were used for data collection and the operation of instrumentation. At the beginning of the deployment, each of the three computer's clocks were synchronized. One computer used MATLAB software to read the sonic anemometer data and control the valve board. A second computer used LabView software to acquire data from the HTDMA. A third computer used LabView software to acquire data from the SMPS and the ambient CPC-1. A multipurpose data acquisition and control board (LabJack U3-LV) was used to control the solenoid valves on the valve board as well as the mode of operation for the HTDMA and SMPS. The LabView software on the second and third computers read a trigger voltage from LabJack and proceeded to execute the corresponding measurement mode.

1.2.6 Back Trajectory Analysis

Past studies have used local wind direction measured by a sonic anemometer in order to separate marine from continentally-influenced air masses on the East Coast of the US [*Norris et al.*, 2008; *de Leeuw et al.*, 2011]. In this study, in addition to the local wind direction, NOAA HYSPLIT [*Stein et al.*, 2015] back trajectories were used to infer the history of the air masses at the measurement location. For each day, hourly back trajectories were obtained for the previous 72 hours for the day of interest. Each hourly back trajectory was manually inspected and the air masses were classified as continental, marine, or undefined. Despite such classification, the air mass origin does not assure that aerosol concentration and number size distribution will be characteristic of that particular environment. For example, Figure 1.3 shows that the majority of the air masses classified as marine followed the eastern seaboard within ~500 km and therefore, may contain continental aerosols. The wind direction from the sonic anemometer data was used to gain further insight into the air mass backtrajectories. From the sonic anemometer data, marine air masses were defined to have local wind direction between the 5 to 210°N sector (comparable to *Norris et al.* [2008] at the same location), while continental air masses were defined as the remainder. Figure 1.4 shows the frequency of wind speed and direction during the deployment and outlines the marine and continental sectors relative to the local geography. Local wind direction from the sonic anemometer was averaged into 3 hour intervals and compared to the HYSPLIT backtrajectories. When the local wind direction was inconsistent with the classification based on the backtrajectory, the air masses were called unclassified (Figure 1.3c).

1.3 RESULTS AND DISCUSSION

1.3.1 Air mass Trajectories

Figure 1.3a and 1.3b show the back trajectories for the air masses that were classified as continental and marine, respectively. During the study period, the air masses with the continental origin reached the research site during the period of 14 May to 16 May. The air masses with marine origin were subdivided into two semi-continuous periods, 29 Apr to 1 May (Marine Period 1) and 9 May to 12 May (Marine Period 2). Figure 3b shows that the air masses during Marine Period 1 originated mostly from over the Northwest Atlantic Ocean and Eastern Canada, while the air masses during Marine Period 2 were circulating near the coastline.

1.3.2 Size Distribution

Figure 1.5 and Table 1.1 summarize the measured aerosol number size distributions for the three periods. According to Figure 1.5, the aerosol size distribution at the site have two modes (best seen for the continental period on Figure 1.5c). The Aitken (dominate) mode diameters are 50.3±0.3 nm (mean±standard error of the mean (SEM)) for Marine Period 1, 66.9±0.8 nm for Marine Period 2, and 49.1±1.7 nm for the continental period. Figure 1.5 also shows that the Aitken mode in the continentally-derived size distribution is larger in number than the Aitken modes in the marine periods. The accumulation mode diameters for the three distributions are 142.8±1.1 nm (mean±SEM) for Marine Period 1, 155.0±2.8 nm for Marine Period 2, and 154.0±3.1 nm for the continental period. Overall, the size distributions associated with Marine Period 1 and Marine Period 2 did not share modal properties consistent with those of traditional “background marine” size distributions [*Wex et al.*, 2016;

Atwood et al., 2017; *Royalty et al.*, submitted]. The background marine distributions were shown to be generally bimodal with both modes contributing equally to the total number concentration. Here the Aitken mode dominates. Nonetheless, observations of Aitken mode dominated size distributions have been described in both remote oceanic environments [e.g., *Tomlinson et al.*, 2007] as well as near maritime sites with continental outflow influence [*Wex et al.*, 2016; *Atwood et al.*, 2017]. If the enhanced Aitken mode can be thought to be a signature for freshly nucleated particles, the variability in the aerosol size distribution between the three modes would indicate that i) all the air masses sampled at the end of the pier were influenced by the continental sources of aerosols, and ii) aging of aerosols over the ocean, near the coastline, caused preferential removal of accumulation mode aerosols, most likely through the wet removal (rain out).

1.3.3 Time Series

Figure 1.6 shows a time series of data collected during the field deployment. Figure 1.6a shows the time series of measured wind speed and direction. According to this figure and the statistics summarized in Table 1.1, there was no considerable variability in the wind speed between the different periods. Table 1.1 shows that the average wind speed was 6.6±2.6 m s^{-1} (mean±std) with the range from 0.5 to 13.7 m s^{-1} during Marine Period 1, 4.4±2.3 m s^{-1} with the range from ~0 to 14.3 m s^{-1} for Marine Period 2, and 5.4±2.0 m s^{-1} with the range from 0.9 to 13.7 m s^{-1} for the continental period.

Figure 1.6b shows that the size distribution modal properties were relatively invariant over time during Marine Period 1 and Marine Period 2. During the continental and the unclassified periods, the size distribution modes often experienced shifts in modal diameter

associated with changes in wind direction. For example, the Aitken mode-dominated size distribution started with an Aitken mode centered at ~20 nm on 6 May. Over time, the concentration shifted to larger mode diameters until reaching a maximum on 9 May.

Figure 1.6c shows the time series of total particle number concentration. According to this figure, number concentrations were fairly stable (~ 2000 cm^{-3}) throughout the deployment, though higher number concentrations (~5000 cm^{-3}) were seen on 2 May and on 15 May and lower numbers were recorded on 5 May. Comparison of Figures 1.6c and 1.6a suggests that variability in particle number concentration was likely associated with the shifts in wind direction. On average, winds blowing from the continental sector were characterized by higher number concentration of particles compared to the winds from the marine sectors. As shown in Table 1.1, the average number concentrations were 1360±22 cm^{-3} (mean±SEM) for Marine Period 1, 1916±41 cm^{-3} for Marine Period 2, and 2429±77 cm^{-3} for the continental period.

The average number concentrations for Marine Periods 1 and Marine Period 2 shown in Figure 1.6c are larger than those of typical clean marine background air [*Heintzenberg et al.*, 2000; *Atwood et al.*, 2017; *Royalty et al.*, submitted] and comparable to that of the continental period. The high number concentration during the Marine Period 1 and Marine Period 2 is likely due to the influence of continental aerosols as discussed in Chapter 1.3.2. Overall, number concentration values at the measurement site (shown in Figure 1.6c and Table 1.1) are comparable to that of rural Southeast US continental aerosol [*Nguyen et al.*, 2014]. Figure 1.6c also shows a comparison between the ambient CPC-1 and the SMPS integrated number concentration between 29 April and 4 May and shows excellent agreement

between the two instruments suggesting closure in between the concentration before and after the SMPS. As mentioned before, the ambient CPC-1 was used in place of a broken CPC-3 starting on 4 May, after which comparison between CPC-1 and the SMPS integrated number concentration was not possible.

Discussion of results from Figures 6d-i will be deferred until later.

1.3.4 Kappa Frequency Distribution

Figure 1.7 shows the κ frequency distributions for the three dry diameters (96, 188, and 284 nm) for Marine Period 1 (Figures 1.7a, 1.7d, and 1.7g), Marine Period 2 (Figures 1.7b, 1.7e, and 1.7h), and the continental period (Figures 1.7c, 1.7f, and 1.7i). Overall, the distributions are dominated by a single mode that spans $\kappa \sim 0.1$ and $\kappa \sim 1$. All of the distributions show a small but distinguishable population at $\kappa < 0.02$, the relative contributions of which is approximately the same during all three periods (Figure 1.7). Table 1.1 summarizes average mode κ values and measurement conditions for the three different periods. Figure 1.7 and Table 1.1 show considerable increase in the mode κ values with increasing dry diameter for Marine Period 1 (from 0.37 to 0.54) and the continental period (from 0.2 to 0.37), while Marine Period 2 exhibits minor changes (from 0.3 to 0.34) in the κ values. In general, the observed range in κ values for the continental air mass are well within the range observed at several continental sites [*Swietlicki et al.*, 2008; *Andreae and Rosenfeld*, 2008; *Nguyen et al.*, 2014] which was attributed to a larger fraction of organic compounds contained in continentally-derived particles [*Jimenez et al.*, 2009]. Interestingly, when comparing Marine Period 1 and the continental period mode κ values for the respective dry diameters (Table 1.1), an increase in the mode κ is always evident from the continental

period to Marine Period 1 (e.g., 0.2 to 0.37 for 96 nm). This increasing mode κ could be explained by different chemical constituents in the air masses. Air masses during Marine Period 1, with higher mode κ values were likely to contain more ocean-derived sodium (more hygroscopic) while the continental air masses are more likely to contain more non-hygroscopic species.

For the Marine Period 1 (Figures 1.7a, 1.7d, and 1.7g), the standard deviation of the entire κ distribution is smaller than for the other two periods. The smaller standard deviation during Marine Period 1 suggests that the particle composition was more homogeneous relative to the other two periods. The 25th and 75th percentile range for Marine Period 1 is also larger than for the other two periods, which may be attributed to smaller number concentrations at the three studied sizes.

1.3.5 Particle Classification

Figures 1.6d-f show the time series of particles classified as sodium-containing, sulfate-like, and carbon-containing in fraction space. During Marine Period 1 (Figure 1.6d) the fraction of particles in the sodium-containing class was -0.02±0.00 (mean±SEM), 0.03±0.01, and 0.08±0.01 for the 96, 188, and 284 nm particles. The negative value for the 96 nm size particles indicates that the concentration was below the limit of detection by the method. The fraction of particles in the sodium-containing class increased with particle diameter and was largest for the 284 nm sized particles. Figures 1.6g-i show the time series when the fraction is weighted by the spectral density (i.e., $\frac{dN}{dlog_{10}D_p}$), obtained from the size distribution at the appropriate diameter. The contribution of particles to the sodium-containing κ class was 29±6 (mean±SEM), and 26±4 cm^{-3} for the 188, and 284 nm particles.

This was the only period that showed positive fractions (i.e. signal) in the sodium-containing class. The fractions for the sodium-containing class during Marine Period 1 are relatively low and thus, the spectral concentrations for 188 and 284 nm sized particles were also low.

Figure 1.6d-f shows that most particles (by fraction and spectral density) were classified as being sulfate-like. During Marine Period 1, the fraction of particles in the sulfate-like class were 0.76±0.01 (mean±SEM), 0.84±0.01, and 0.76±0.01 for the 96, 188, and 284 nm particles, respectively. When weighted by the spectral density, the contribution of particles to the sulfate-like class was 1098±46 (mean±SEM), 881±23, and 262±10 cm^{-3} for the 96, 188, and 284 nm particles, respectively. The concentration decreased with increasing particle size, consistent with the size distribution for this period which showed a larger number of particles at smaller sizes (Figure 1.5a). During Marine Period 2, the fraction of particles in the sulfate-like class was 0.82±0.01 (mean±SEM), 0.85±0.01, and 0.77±0.01 for the 96, 188, and 284 nm particles, respectively. When weighted by the spectral density, the contribution of particles to the sulfate-like class was 3820±72 (mean±SEM), 2165±72, and 857±20 cm^{-3} for the 96, 188, and 284 nm particles, respectively. Again, the concentration decreased with increasing particle size; however, larger in magnitude than in Marine Period 1. During the continental period (14 to 16 May) the fraction of particles falling within the sulfate-like class was 0.64±0.02 (mean±SEM), 0.84±0.01, and 0.81±0.01 for the 96, 188, and 284 nm particles, respectively. When weighted by the spectral density, the contribution of particles to the sulfate-like class was 1827±60 (mean±SEM), 2052±56, and 741±56 cm^{-3} for the 96, 188, and 284 nm particles, respectively. This period had the largest spectral concentration for the 188 nm sized particles, followed by the 96 and then the 284 nm sized

particles. This observation is consistent with the number concentration for the SMPS during the continental period being more dominant for smaller sizes (Figure 1.5c).

During Marine Period 1 the fraction of particles in the carbon-containing class was 0.26±0.01 (mean±SEM), 0.13±0.01, and 0.16±0.01 for the 96, 188, and 284 nm particles, respectively. When weighted by the spectral density, the contribution of particles to the carbon-containing class was 534±46 (mean±SEM), 141±12, and 52±5 cm^{-3} for the 96, 188, and 284 nm particles, respectively. During Marine Period 2, the fraction of particles in the carbon-containing class was 0.21±0.01 (mean±SEM), 0.18±0.01, and 0.26±0.01 for the 96, 188, and 284 nm particles, respectively. When weighted by the spectral density, the contribution of particles to the carbon-containing class was 1038±48 (mean±SEM), 456±31, and 308±16 cm^{-3} for the 96, 188, and 284 nm particles, respectively. During the continental period the fraction of particles in the carbon-containing class was 0.38±0.02 (mean±SEM), 0.18±0.01, and 0.22±0.01 for the 96, 188, and 284 nm particles, respectively. When weighted by the spectral density, the contribution of particles to the carbon-containing particle class was 1368±94 (mean±SEM), 495±40, and 221±21 cm^{-3} for the 96, 188, and 284 nm particles, respectively. The spectral concentrations for each of the three periods increased with particle diameter; consistent with the size distributions that show decreasing concentrations across those sizes.

An interesting observation from using this technique was that while spectral concentrations of sulfate-like particles were persistently higher than the carbon-containing spectral concentration during the marine periods, the carbon-containing spectral concentration during Marine Period 2 was higher on average than Marine Period 1 (Table

1.1). A possible explanation for this observation could be that continental outflow originating from the Southeastern US influenced the recirculating air (shown in Figure 1.3b) during Marine Period 2. Observations suggest production of both primary and secondary organic aerosol occur at higher rates in the Southeastern versus the Northeastern US during spring [*Yu et al.*, 2007; *García et al.*, 2017]. As such, the recirculating trajectories during Marine Period 2 may have been influenced by outflow originating in the US and transporting across the Southeastern US and thus, could have a higher loading of carbonaceous aerosol. Mesoscale circulation models suggest that the Southeastern US represents a major site of continental outflow for continental US pollution [*Li et al.*, 2005]. HYSPLIT suggests the majority of the air masses sampled during Marine Period 1 either originated offshore of the Northeastern US or in the vicinity of the Sargasso Sea. These air masses during Marine Period 1 traveled for a long time along trajectories over the ocean where cloud processing could account for the change in the carbonaceous aerosols.

1.4 CONCLUSIONS

Overall, this set of observations create an interesting picture highlighting the dynamics of continental outflow in the Southeastern US. More specifically, a number of studies, both new and old, present evidence suggesting the contribution of primary marine aerosol to the marine aerosol number budget is only minor [*Woodcock*, 1952; *Modini et al.*, 2015; *Royalty et al.*, 2017]. More so, it is becoming more clear that the number budget in remote marine environments is controlled by influences of continental sources [e.g. *Andreae*, 2007; *Quinn and Bates*, 2011; *Clarke et al.*, 2013]. As such, it is important to have a better characterization of aerosol properties associated with continental outflow to better understand

processes leading to the observed low cloud condensation nuclei concentrations in remote regions of the oceans [*Wood et al.,* 2017]. The work presented here provides a two-week data set of aerosol size and hygroscopicity data in a coastal Southeastern US sampling site which provides useful data in a region that is often times difficult to obtain accurate modeling result.

Table 1.1**:** Summarized campaign concentration statistics for SMPS, Ambient CPC and HTDMA.

		Marine Period 1			Marine Period 2			Continental Period		
Dry Diameter (nm)		96	188	284	96	188	284	96	188	284
Kappa Distributions	Mode κ (Mean±SEM)	0.37±0.01	0.45±0.01	0.54±0.03	0.30±0.01	0.34±0.01	0.29±0.01	0.20±0.01	0.36±0.01	0.37±0.02
	RH (%) (Mean±SEM)	80.6±0.1	80.6±0.1	80.5±0.1	79.4±0.1	79.4±0.2	79.4±0.1	76.8±0.2	76.6±0.2	77.0±0.3
	n	176	123	117	203	132	133	94	67	64
Fraction	Sodium-containing	-0.02±0.00	0.03±0.01	0.08±0.01	-0.03±0.00	-0.03±0.00	-0.03±0.00	-0.02±0.00	-0.03±0.00	-0.03±0.00
	Sulfate-like	0.76±0.01	0.84±0.01	0.76±0.01	0.82±0.01	0.85±0.01	0.77±0.01	0.64±0.02	0.84±0.01	0.81±0.01
	Carbon-containing	0.26±0.01	0.13±0.01	0.15±0.01	0.21±0.01	0.18±0.01	0.26±0.01	0.38±0.02	0.18±0.01	0.22±0.01
Spectral Concentration (cm^{-3})	Sodium-containing	-42±3	29±6	26±4	-150±3	-86±3	-37±2	-71±6	-71±5	-29±4
	Sulfate-like	1098±46	881±23	262±10	3820±72	2165±72	857±20	1827±60	2052±56	741±56
	Carbon-containing	534±46	141±12	52±5	1038±48	456±31	308±16	1368±94	495±40	221±21
SMPS Distributions	Aiken Mode (nm) (Mean±SEM)	50.3±0.3			66.9±0.8			49.1±1.7		
	Accumulation Mode (nm) (Mean±SEM)	142.8±1.1			155.0±2.8			154.0±3.1		
	Integrated Concentration (cm^{-3})	1360±22			1916±41			2429±77		
	n	376			78			77		
Wind Speed	Mean±STD ($m\ s^{-1}$)	6.6±2.6			4.4±2.3			5.4±2.0		
	Maximum ($m\ s^{-1}$)	13.7			14.3			13.7		
	Minimum ($m\ s^{-1}$)	0.5			0			0.9		
	n	157739			195746			95867		

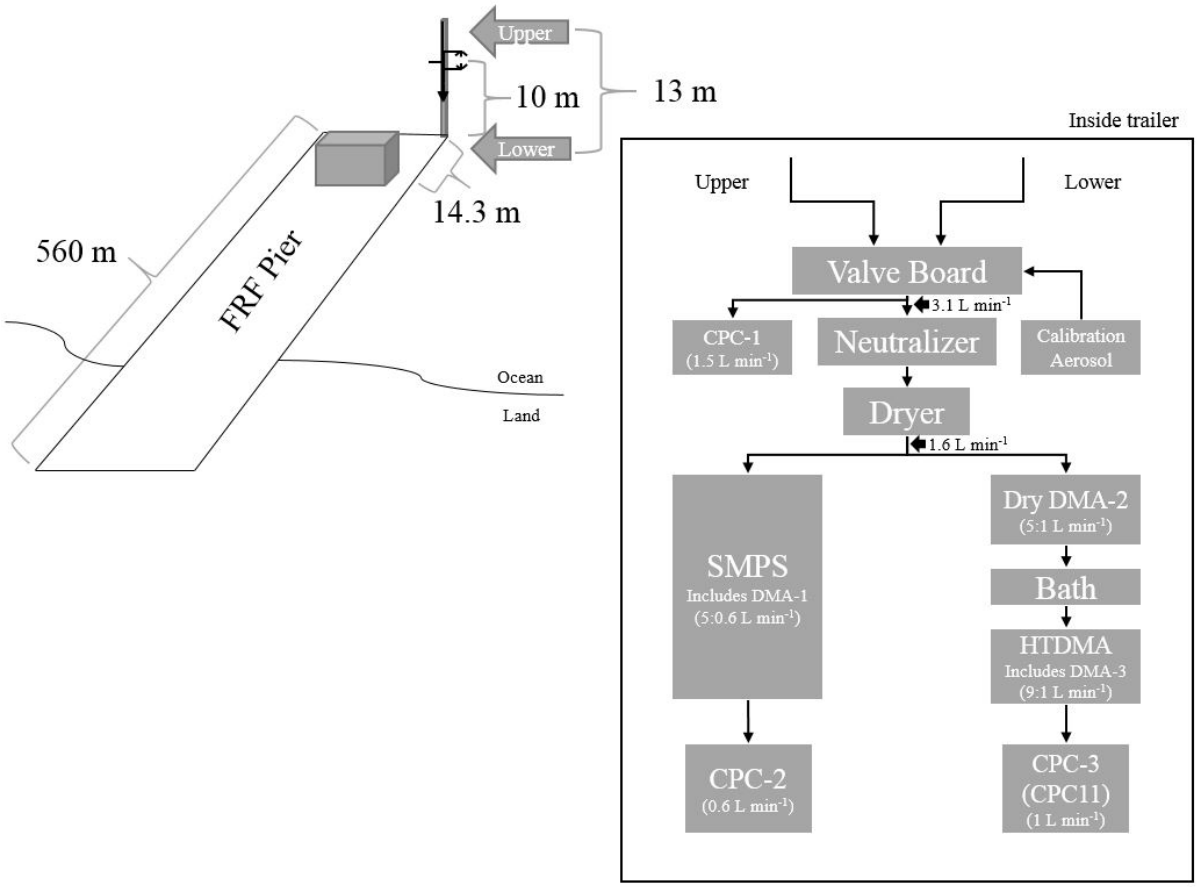

Figure 1.1 Schematic of the instrument set up.

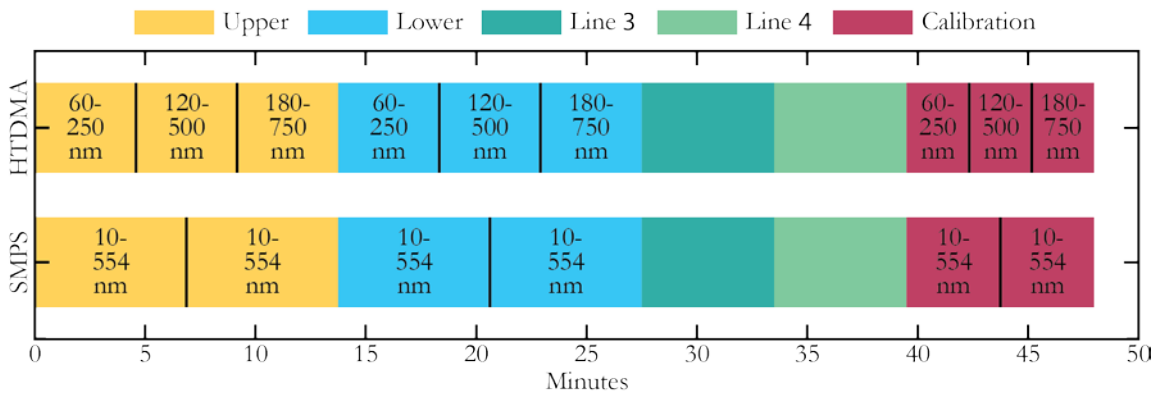

Figure 1.2 The time series of valve and instrument operation for one duty cycle for HTDMA (top) and SMPS (bottom). Colors indication which valve was open.

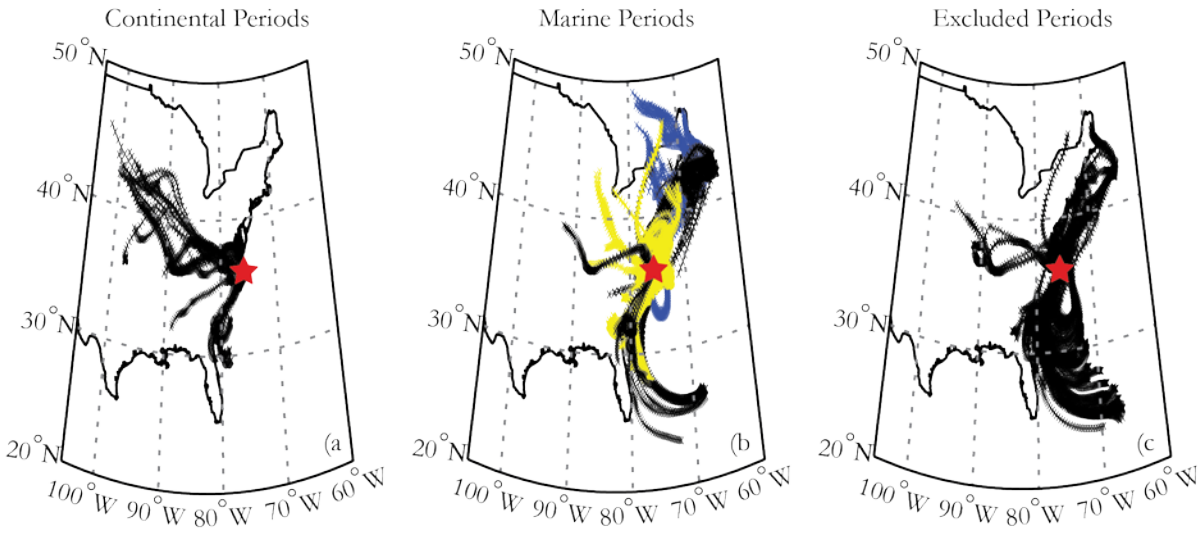

Figure 1.3 Back trajectories for air mass classifications, (a continental, (b marine, and (c excluded due to local circulation. The two marine periods are colored blue and yellow for Marine Period 1 and 2, respectively. The red star is centered on Duck, North Carolina.

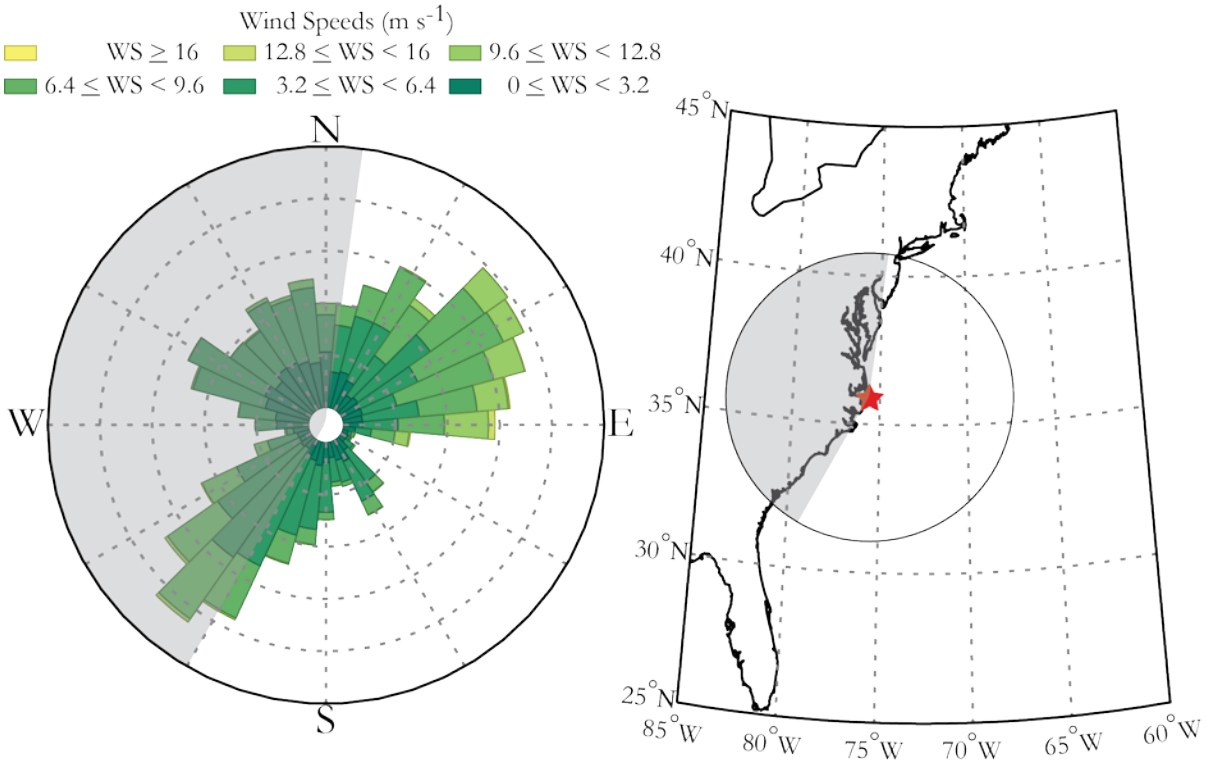

Figure 1.4 (Left) Wind rose showing the frequency of speed and direction during the deployment. (Right) Wind sector with continental section shaded in gray. The red star is centered on Duck, North Carolina.

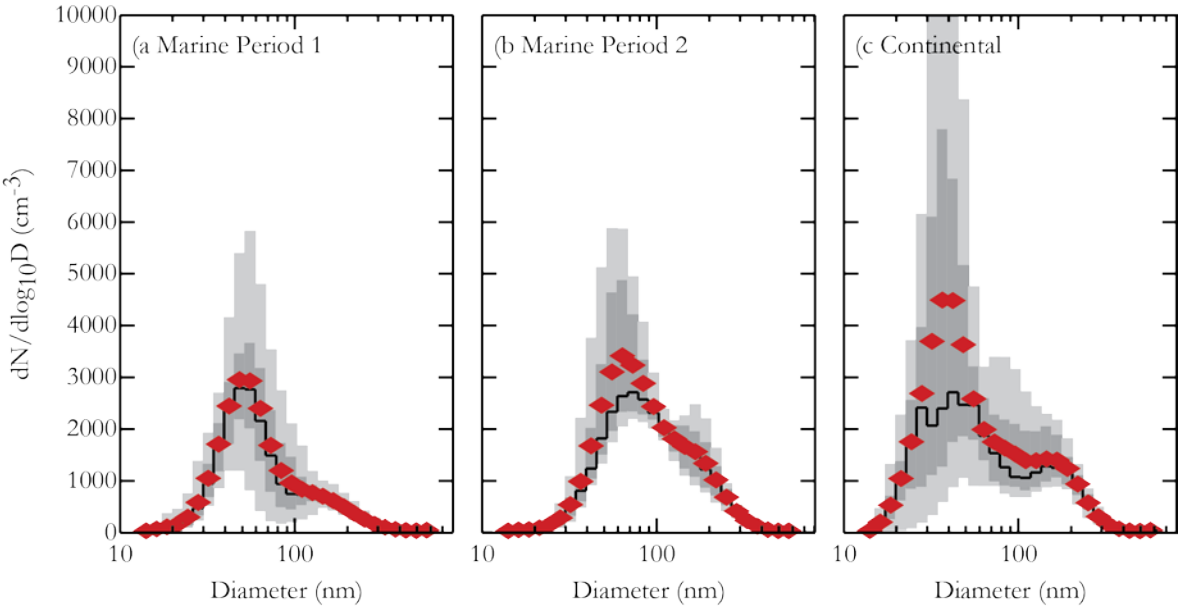

Figure 1.5 The SMPS number size distributions for (a. Marine Period 1, (b. Marine Period 2, and the (c. continental period. The mean number concentration for each diameter bin is indicated by the red diamonds. The median number concentration for each diameter bin is indicated by the black line. The dark gray shading indicates the 25th and 75th percentiles. The light gray shading indicates the 5th and 95th percentiles.

Figure 1.6 Time series summary of the deployment. Gaps in the data indicate that the instrument was sampling on a mode not mentioned here or that the instrument was down. Top to bottom: (a) Wind speed (orange) and direction (brown). Wind blowing from the continental sector is shaded in gray; (b) aerosol size distribution; colors represent spectral concentration; (c) Total particle concentration from the ambient CPC-1 (gold) and from the (Figure 1.6 continued) SMPS integrated dry size distribution (purple). The Marine Period 1 and 2 are shaded in blue and the continental period is shaded in green; (d) Fraction of particles in the sodium-containing class. Colored markers distinguish the dry particle diameter as shown in the legend. Average fractions are indicated by the lines; (e) Fraction of particles in the sulfate-like class; (f) Fraction of particles in the carbon-containing class; (g) Estimated spectral concentration of particles in the sodium-containing class; (h) Estimated spectral concentration of particles in the sulfate-like class; (i) Estimated spectral concentration of particles in the carbon-containing class.

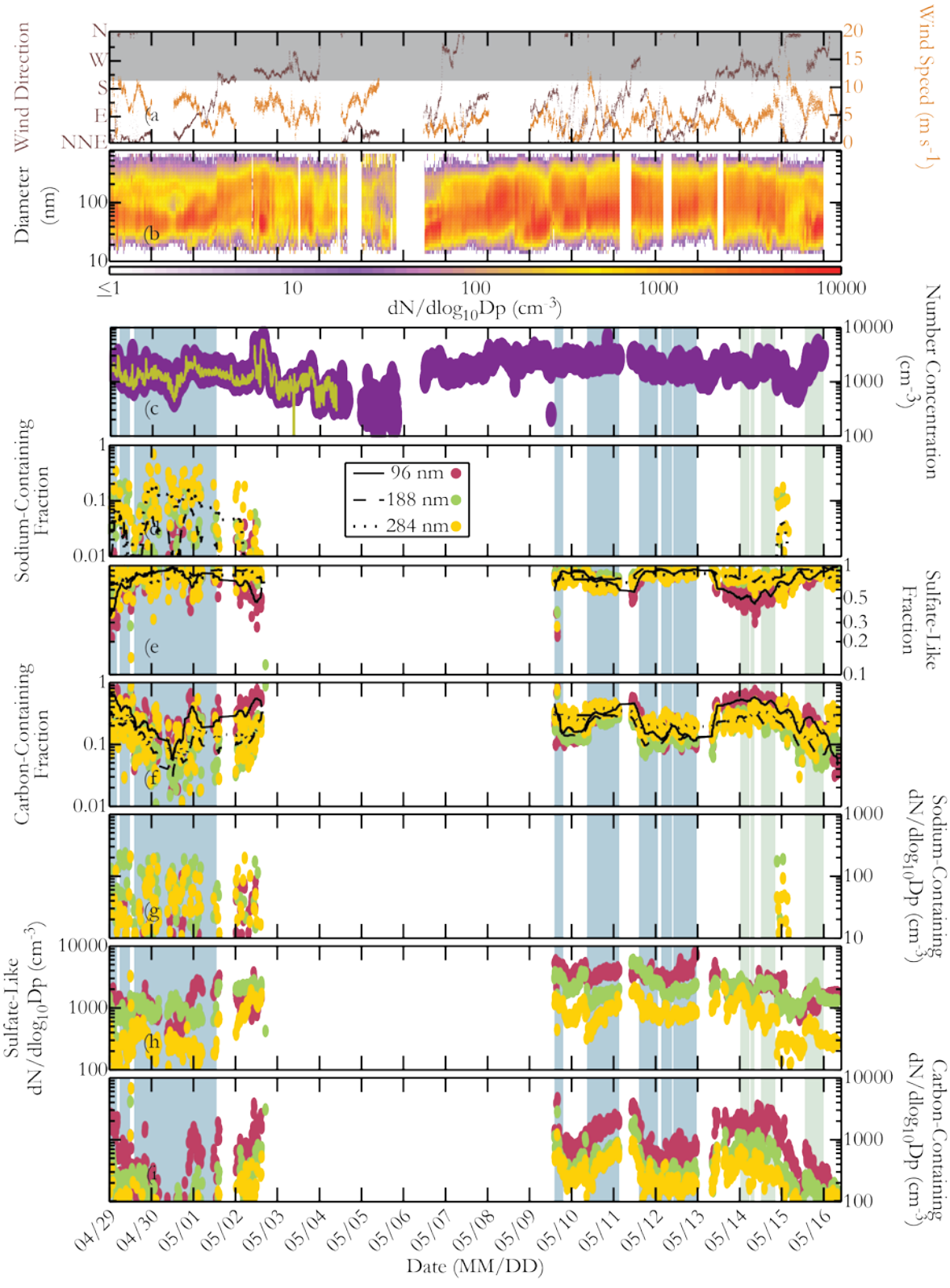
Wind Direction
N
W
S
E
NNE
(a)
Wind Speed (m s^{-1})
20
15
10
5
0
Diameter (nm)
100
10
(b)
≤1
10
100
1000
10000
dN/dlog$_{10}$Dp (cm^{-3})
Number Concentration (cm^{-3})
10000
1000
100
(c)
Sodium-Containing Fraction
1
0.1
0.01
(d)
96 nm
-188 nm
284 nm
Sulfate-Like Fraction
1
0.5
0.3
0.2
0.1
(e)
Carbon-Containing Fraction
1
0.1
0.01
(f)
Sodium-Containing dN/dlog$_{10}$Dp (cm^{-3})
1000
100
10
(g)
Sulfate-Like dN/dlog$_{10}$Dp (cm^{-3})
10000
1000
100
(h)
Carbon-Containing dN/dlog$_{10}$Dp (cm^{-3})
10000
1000
100
(i)
04/29
04/30
05/01
05/02
05/03
05/04
05/05
05/06
05/07
05/08
05/09
05/10
05/11
05/12
05/13
05/14
05/15
05/16
Date (MM/DD)

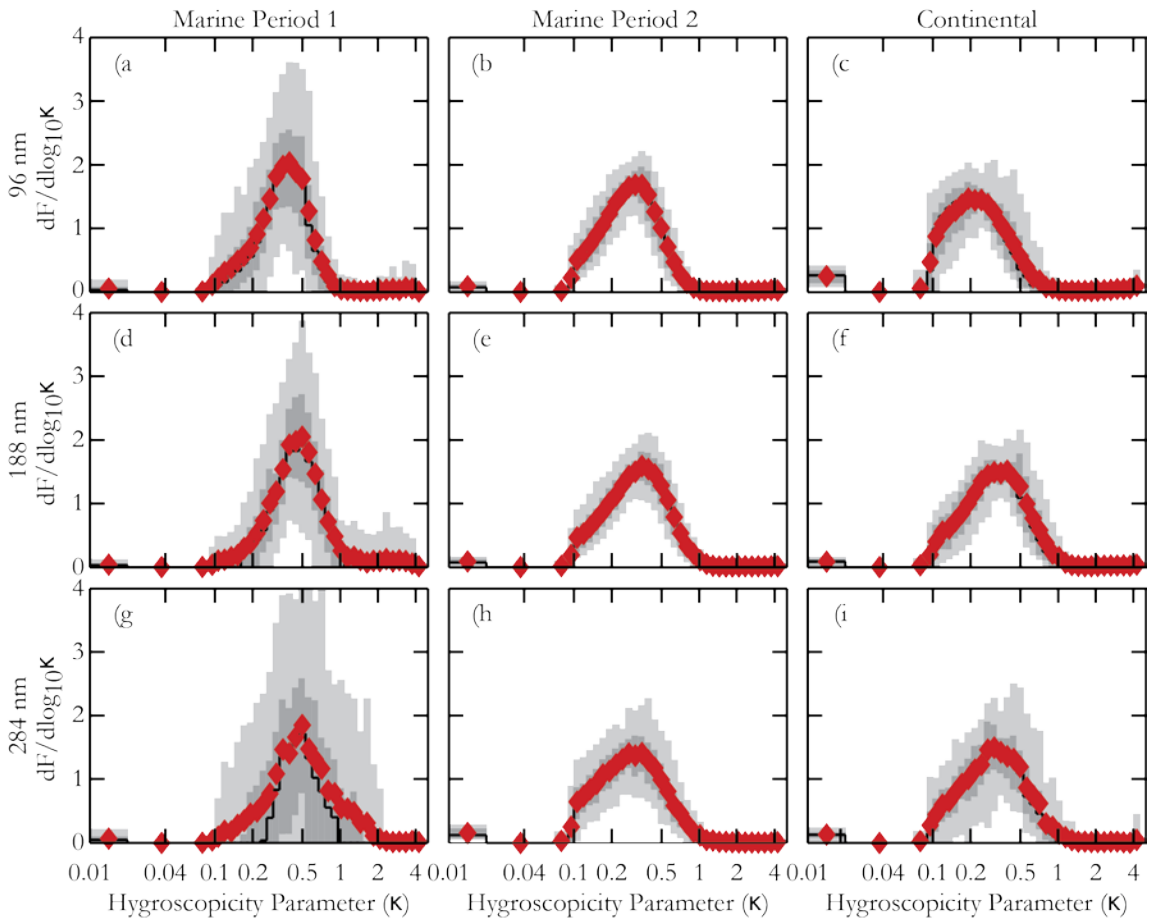

Figure 1.7 The kappa frequency distributions for the three air mass periods and each of the three dry diameters (96, 188, and 284 nm). The mean frequency for each kappa bin is indicated by the red diamonds. The median frequency for each kappa bin is indicated by the solid black line. The dark gray shading indicates the 25th and 75th percentiles. The light gray shading indicates the 5th and 95th percentiles.

CHAPTER 2

2.1 FUTURE DIRECTIONS

Looking forward, there are three paths that can be taken with the research presented here; further validation of the particle classification method, comparison of the observation shown here to regional air quality models, and the incorporation of the particle classification method into a flux measurement system.

The particle classification method used here, of *Royalty et al.* [submitted], requires further validation. This validation of the method should include laboratory analysis of externally mixed aerosols of different chemical constituents (ammonium sulfate, sodium chloride, organic compounds, etc.). These external mixtures should be produced in varying ratios. The particle classification method should then be used to determine the relative fraction of each constituent. If it works properly, the method should be able to discern the approximate relative fraction of each chemical constituent. In conjunction with these experiments, the method should be tested for a detection limit, i.e. the fraction at which the method cannot distinguish between chemical constituents.

The observations presented here, of HTDMA and SMPS measurements at a coastal site, would be interesting to compare to regional air quality model for validation purposes. As an example, the Community Multi-scale Air Quality (CMAQ) model is an atmospheric dispersion model developed to understand air pollution. Parameterizations for surf zone production of sea-spray aerosol have been recently updated for CMAQ [*Gantt et al.*, 2015]. The method provided here could possibly be used for comparing predicted sea-spray aerosol number concentrations and observations. The SMPS number concentration measurements

could be compared to the concentration outputs from CMAQ for the same location and time. The detailed chemical composition output from CMAQ can be compared to the fractions determined using the particle classification method.

The research presented here was collected alongside the ongoing development and testing of a particle flux measurement system. A Relaxed Eddy Accumulation (REA) flux measurement system, using an HTDMA system similar to the one described here, is currently being tested at the US Environmental Protection Agency's aerosol wind tunnel in Durham, North Carolina. Briefly, the principle behind REA particle fluxes is that the flux is calculated as the concentration difference between updrafts and downdrafts. A positive value indicates a net upward flux of particles and a negative value indicates a net downward flux of particles. The updrafts and downdrafts are determined by a sonic anemometer. The sonic anemometer measures the standard deviation in the vertical wind component at 10 Hz. When the average standard deviation (calculated continuously) in the vertical component exceeds a predefined threshold the corresponding draft is sampled (updraft for a positive threshold and downdraft for a negative threshold). The predefined threshold is reported to be within the range of 0.4-0.6 in the literature (REF), and represents a deadband where the atmospheric eddies are below a certain magnitude. It is common when using the REA method to measure updrafts and downdrafts simultaneously. This is typically done one of two ways; (1 by measuring the updrafts and downdrafts in separate but identical measurement units, or (2 through the sampling the updrafts and downdrafts into separate containers for analysis later. The REA particle flux method used here samples into separate containers, or more specifically barrels, to be measured later. The drafts in each barrel are then sampled into the HTDMA system. By

obtaining the hygroscopicity or growth factor distribution, the particle classification method can then be used on each barrel to determine the different fractions of each class in the updrafts and downdrafts. This would result in flux measurements of sodium-containing, sulfate-like, and carbon-containing particles.

As such, the work presented within this Masters Thesis provides a foundation for multiple avenues for further research.

REFERENCES

Birkemeier, W. A., H. C. Miller, S. D. Wilhelm, A. E. DeWall, and C. S. Gorbics (1985), A User's guide to the Coastal Engineering Research Centers (CERC's) field research facility, *Misc. Rep. CERC-85-1*, U. S. Army Eng. Waterw. Exp. Stn., Vicksburg, MS.

Andreae, M. O. (2007), Aerosols Before Pollution, *Science*, *315*(5808), 50–51, doi:10.1126/science.1136529.

Andreae, M. O., and D. Rosenfeld (2008), Aerosol–cloud–precipitation interactions. Part 1. The nature and sources of cloud-active aerosols, *Earth-Sci. Rev.*, *89*(1–2), 13–41, doi:10.1016/j.earscirev.2008.03.001.

Asmi, E., A. Frey, A. Virkkula, M. Ehn, H. E. Manninen, H. Timonen, O. Tolonen-Kivimäki, M. Aurela, R. Hillamo, and M. Kulmala (2010), Hygroscopicity and chemical composition of Antarctic sub-micrometre aerosol particles and observations of new particle formation, *Atmos Chem Phys*, *10*(9), 4253–4271, doi:10.5194/acp-10-4253-2010.

Atwood, S. A., J. S. Reid, S. M. Kreidenweis, D. R. Blake, H. H. Jonsson, N. D. Lagrosas, P. Xian, E. A. Reid, W. R. Sessions, and J. B. Simpas (2017), Size-resolved aerosol and cloud condensation nuclei (CCN) properties in the remote marine South China Sea – Part 1: Observations and source classification, *Atmos Chem Phys*, *17*(2), 1105–1123, doi:10.5194/acp-17-1105-2017.

Backer, L. C., B. Kirkpatrick, L. E. Fleming, Y. S. Cheng, R. Pierce, J. A. Bean, R. Clark, D. Johnson, A. Wanner, R. Tamer, Y. Zhou, and D. G. Baden (2005), Occupational Exposure to Aerosolized Brevetoxins during Florida Red Tide Events: Effects on a Healthy Worker Population, *Environ. Health Perspect.*, *113*(5), 644–649, doi:10.1289/ehp.7502.

Berg, O. H., E. Swietlicki, and R. Krejci (1998), Hygroscopic growth of aerosol particles in the marine boundary layer over the Pacific and Southern Oceans during the First Aerosol Characterization Experiment (ACE 1), *J. Geophys. Res. Atmospheres*, *103*(D13), 16535–16545, doi:10.1029/97JD02851.

Carslaw, K. S., L. A. Lee, C. L. Reddington, K. J. Pringle, A. Rap, P. M. Forster, G. W. Mann, D. V. Spracklen, M. T. Woodhouse, L. A. Regayre, and J. R. Pierce (2013), Large contribution of natural aerosols to uncertainty in indirect forcing, *Nat. Lond.*, *503*(7474), 67–71.

Cheng, Y. S., Y. Zhou, C. M. Irvin, R. H. Pierce, J. Naar, L. C. Backer, L. E. Fleming, B. Kirkpatrick, and D. G. Baden (2005), Characterization of Marine Aerosol for

Assessment of Human Exposure to Brevetoxins, *Environ. Health Perspect.*, *113*(5), 638–643, doi:10.1289/ehp.7496.

Clarke, A. D., S. Freitag, R. M. C. Simpson, J. G. Hudson, S. G. Howell, V. L. Brekhovskikh, T. Campos, V. N. Kapustin, and J. Zhou (2013), Free troposphere as a major source of CCN for the equatorial pacific boundary layer: long-range transport and teleconnections, *Atmos Chem Phys*, *13*(15), 7511–7529, doi:10.5194/acp-13-7511-2013.

Dawson, K. W., M. D. Petters, N. Meskhidze, S. S. Petters, and S. M. Kreidenweis (2016), Hygroscopic growth and cloud droplet activation of xanthan gum as a proxy for marine hydrogels, *J. Geophys. Res. Atmospheres*, *121*(19), 2016JD025143, doi:10.1002/2016JD025143.

Gantt, B., M. S. Johnson, N. Meskhidze, J. Sciare, J. Ovadnevaite, D. Ceburnis, and C. D. O'Dowd (2012), Model evaluation of marine primary organic aerosol emission schemes, *Atmos Chem Phys*, *12*(18), 8553–8566, doi:10.5194/acp-12-8553-2012.

Gantt, B., J. T. Kelly, and J. O. Bash (2015), Updating sea spray aerosol emissions in the Community Multiscale Air Quality (CMAQ) model version 5.0.2, *Geosci Model Dev*, *8*(11), 3733–3746, doi:10.5194/gmd-8-3733-2015.

García, M. I., S. Rodríguez, and A. Alastuey (2017), Impact of North America on the aerosol composition in the North Atlantic free troposphere, *Atmos Chem Phys Discuss*, *2017*, 1–31, doi:10.5194/acp-2017-60.

Heintzenberg, J., D. C. Covert, and R. V. Dingenen (2000), Size distribution and chemical composition of marine aerosols: a compilation and review, *Tellus B*, *52*(4), doi:10.3402/tellusb.v52i4.17090.

Hersey, S. P., A. Sorooshian, S. M. Murphy, R. C. Flagan, and J. H. Seinfeld (2009), Aerosol hygroscopicity in the marine atmosphere: a closure study using high-time-resolution, multiple-RH DASH-SP and size-resolved C-ToF-AMS data, *Atmos Chem Phys*, *9*(7), 2543–2554, doi:10.5194/acp-9-2543-2009.

Hoose, C., J. E. Kristjánsson, T. Iversen, A. Kirkevåg, Ø. Seland, and A. Gettelman (2009), Constraining cloud droplet number concentration in GCMs suppresses the aerosol indirect effect, *Geophys. Res. Lett.*, *36*(12), L12807, doi:10.1029/2009GL038568.

Jickells, T. D., A. R. Baker, and R. Chance (2016), Atmospheric transport of trace elements and nutrients to the oceans, *Phil Trans R Soc A*, *374*(2081), 20150286, doi:10.1098/rsta.2015.0286.

Jimenez, J. L., M. R. Canagaratna, N. M. Donahue, A. S. H. Prevot, Q. Zhang, J. H. Kroll, P. F. DeCarlo, J. D. Allan, H. Coe, N. L. Ng, A. C. Aiken, K. S. Docherty, I. M.

Ulbrich, A. P. Grieshop, A. L. Robinson, J. Duplissy, J. D. Smith, K. R. Wilson, V. A. Lanz, C. Hueglin, Y. L. Sun, J. Tian, A. Laaksonen, T. Raatikainen, J. Rautiainen, P. Vaattovaara, M. Ehn, M. Kulmala, J. M. Tomlinson, D. R. Collins, M. J. Cubison, E, J. Dunlea, J. A. Huffman, T. B. Onasch, M. R. Alfarra, P. I. Williams, K. Bower, Y. Kondo, J. Schneider, F. Drewnick, S. Borrmann, S. Weimer, K. Demerjian, D. Salcedo, L. Cottrell, R. Griffin, A. Takami, T. Miyoshi, S. Hatakeyama, A. Shimono, J. Y. Sun, Y. M. Zhang, K. Dzepina, J. R. Kimmel, D. Sueper, J. T. Jayne, S. C. Herndon, A. M. Trimborn, L. R. Williams, E. C. Wood, A. M. Middlebrook, C. E. Kolb, U. Baltensperger, and D. R. Worsnop (2009), Evolution of Organic Aerosols in the Atmosphere, *Science*, *326*(5959), 1525–1529, doi:10.1126/science.1180353.

Kim, G., H. Cho, A. Seo, D. Kim, Y. Gim, B. Y. Lee, Y. J. Yoon, and K. Park (2015), Comparison of Hygroscopicity, Volatility, and Mixing State of Submicrometer Particles between Cruises over the Arctic Ocean and the Pacific Ocean, *Environ. Sci. Technol.*, *49*(20), 12024–12035, doi:10.1021/acs.est.5b01505.

de Leeuw, G., E. L. Andreas, M. D. Anguelova, C. W. Fairall, E. R. Lewis, C. O'Dowd, M. Schulz, and S. E. Schwartz (2011), Production flux of sea spray aerosol, *Rev. Geophys.*, *49*(2), RG2001, doi:10.1029/2010RG000349.

Li, Q., D. J. Jacob, R. Park, Y. Wang, C. L. Heald, R. Hudman, R. M. Yantosca, R. V. Martin, and M. Evans (2005), North American pollution outflow and the trapping of convectively lifted pollution by upper-level anticyclone, *J. Geophys. Res. Atmospheres*, *110*(D10), D10301, doi:10.1029/2004JD005039.

Lohmann, U., J. Feichter, J. Penner, and R. Leaitch (2000), Indirect effect of sulfate and carbonaceous aerosols: A mechanistic treatment, *J. Geophys. Res. Atmospheres*, *105*(D10), 12193–12206, doi:10.1029/1999JD901199.

Massling, A., A. Wiedensohler, B. Busch, C. Neusü\s s, P. Quinn, T. Bates, and D. Covert (2003), Hygroscopic properties of different aerosol types over the Atlantic and Indian Oceans, *Atmospheric Chem. Phys.*, *3*(5), 1377–1397.

Massling, A., S. Leinert, A. Wiedensohler, and D. Covert (2007), Hygroscopic growth of sub-micrometer and one-micrometer aerosol particles measured during ACE-Asia, *Atmos Chem Phys*, *7*(12), 3249–3259, doi:10.5194/acp-7-3249-2007.

Mochida, M., C. Nishita-Hara, H. Furutani, Y. Miyazaki, J. Jung, K. Kawamura, and M. Uematsu (2011), Hygroscopicity and cloud condensation nucleus activity of marine aerosol particles over the western North Pacific, *J. Geophys. Res. Atmospheres*, *116*(D6), D06204, doi:10.1029/2010JD014759.

Modini, R. L., A. A. Frossard, L. Ahlm, L. M. Russell, C. E. Corrigan, G. C. Roberts, L. N. Hawkins, J. C. Schroder, A. K. Bertram, R. Zhao, A. K. Y. Lee, J. P. D. Abbatt, J.

Lin, A. Nenes, Z. Wang, A. Wonaschütz, A. Sorooshian, K. J. Noone, H. Jonsson, J. H. Seinfeld, D. Toom-Sauntry, A. M. Macdonald, and W. R. Leaitch (2015), Primary marine aerosol-cloud interactions off the coast of California, *J. Geophys. Res. Atmospheres*, *120*(9), 2014JD022963, doi:10.1002/2014JD022963.

Nguyen, T. K. V., M. D. Petters, S. R. Suda, H. Guo, R. J. Weber, and A. G. Carlton (2014), Trends in particle-phase liquid water during the Southern Oxidant and Aerosol Study, *Atmos Chem Phys*, *14*(20), 10911–10930, doi:10.5194/acp-14-10911-2014.

Norris, S. J., I. M. Brooks, G. de Leeuw, M. H. Smith, M. Moerman, and J. J. N. Lingard (2008), Eddy covariance measurements of sea spray particles over the Atlantic Ocean, *Atmos Chem Phys*, *8*(3), 555–563, doi:10.5194/acp-8-555-2008.

Ovadnevaite, J., A. Manders, G. de Leeuw, D. Ceburnis, C. Monahan, A.-I. Partanen, H. Korhonen, and C. D. O'Dowd (2014), A sea spray aerosol flux parameterization encapsulating wave state, *Atmos Chem Phys*, *14*(4), 1837–1852, doi:10.5194/acp-14-1837-2014.

Petters, M. D., and S. M. Kreidenweis (2007), A single parameter representation of hygroscopic growth and cloud condensation nucleus activity, *Atmos Chem Phys*, *7*(8), 1961–1971, doi:10.5194/acp-7-1961-2007.

Petters, M. D., C. M. Carrico, S. M. Kreidenweis, A. J. Prenni, P. J. DeMott, J. L. Collett, and H. Moosmüller (2009), Cloud condensation nucleation activity of biomass burning aerosol, *J. Geophys. Res. Atmospheres*, *114*(D22), D22205, doi:10.1029/2009JD012353.

Quinn, P. K., and T. S. Bates (2011), The case against climate regulation via oceanic phytoplankton sulphur emissions, *Nature*, *480*(7375), 51–56, doi:10.1038/nature10580.

Rader, D. J., and P. H. McMurry (1986), Application of the tandem differential mobility analyzer to studies of droplet growth or evaporation, *J. Aerosol Sci.*, *17*(5), 771–787, doi:10.1016/0021-8502(86)90031-5.

Sarwar, G., B. Gantt, D. Schwede, K. Foley, R. Mathur, and A. Saiz-Lopez (2015), Impact of Enhanced Ozone Deposition and Halogen Chemistry on Tropospheric Ozone over the Northern Hemisphere, *Environ. Sci. Technol.*, *49*(15), 9203–9211, doi:10.1021/acs.est.5b01657.

Snider, J. R., and M. D. Petters (2008), Optical particle counter measurement of marine aerosol hygroscopic growth, *Atmos Chem Phys*, *8*(7), 1949–1962, doi:10.5194/acp-8-1949-2008.

Stein, A. F., R. R. Draxler, G. D. Rolph, B. J. B. Stunder, M. D. Cohen, and F. Ngan (2015), NOAA's HYSPLIT Atmospheric Transport and Dispersion Modeling System, *Bull. Am. Meteorol. Soc.*, *96*(12), 2059–2077, doi:10.1175/BAMS-D-14-00110.1.

Stolzenburg, M., N. Kreisberg, and S. Hering (1998), Atmospheric Size Distributions Measured by Differential Mobility Optical Particle Size Spectrometry, *Aerosol Sci. Technol.*, *29*(5), 402–418, doi:10.1080/02786829808965579.

Suda, S. R., and M. D. Petters (2013), Accurate Determination of Aerosol Activity Coefficients at Relative Humidities up to 99% Using the Hygroscopicity Tandem Differential Mobility Analyzer Technique, *Aerosol Sci. Technol.*, *47*(9), 991–1000, doi:10.1080/02786826.2013.807906.

Swietlicki, E., J. Zhou, D. S. Covert, K. Hämeri, B. Busch, M. Väkeva, U. Dusek, O. H. Berg, A. Wiedensohler, P. Aalto, J. Mäkelä, B. G. Martinsson, G. Papaspiropoulos, B. Mentes, G. Frank, and F. Stratmann (2000), Hygroscopic properties of aerosol particles in the north-eastern Atlantic during ACE-2, *Tellus B*, *52*(2), doi:10.3402/tellusb.v52i2.16093.

Swietlicki, E., H.-C. Hansson, K. Hämeri, B. Svenningsson, A. Massling, G. Mcfiggans, P. H. Mcmurry, T. Petäjä, P. Tunved, M. Gysel, D. Topping, E. Weingartner, U. Baltensperger, J. Rissler, A. Wiedensohler, and M. Kulmala (2008), Hygroscopic properties of submicrometer atmospheric aerosol particles measured with H-TDMA instruments in various environments—a review, *Tellus B*, *60*(3), 432–469, doi:10.1111/j.1600-0889.2008.00350.x.

Tomlinson, J. M., R. Li, and D. R. Collins (2007), Physical and chemical properties of the aerosol within the southeastern Pacific marine boundary layer, *J. Geophys. Res. Atmospheres*, *112*(D12), D12211, doi:10.1029/2006JD007771.

Vignati, E., G. de Leeuw, and R. Berkowicz (2001), Modeling coastal aerosol transport and effects of surf-produced aerosols on processes in the marine atmospheric boundary layer, *J. Geophys. Res. Atmospheres*, *106*(D17), 20225–20238, doi:10.1029/2000JD000025.

Wang, M., and J. E. Penner (2009), Aerosol indirect forcing in a global model with particle nucleation, *Atmos Chem Phys*, *9*(1), 239–260, doi:10.5194/acp-9-239-2009.

Wang, S. C., and R. C. Flagan (1990), Scanning Electrical Mobility Spectrometer, *Aerosol Sci. Technol.*, *13*(2), 230–240, doi:10.1080/02786829008959441.

Wex, H., K. Dieckmann, G. C. Roberts, T. Conrath, M. A. Izaguirre, S. Hartmann, P. Herenz, M. Schäfer, F. Ditas, T. Schmeissner, S. Henning, B. Wehner, H. Siebert, and F. Stratmann (2016), Aerosol arriving on the Caribbean island of Barbados: physical

properties and origin, *Atmos Chem Phys*, *16*(22), 14107–14130, doi:10.5194/acp-16-14107-2016.

Wood, R., J. D. Stemmler, J. Rémillard, and A. Jefferson (2017), Low-CCN concentration air masses over the eastern North Atlantic: Seasonality, meteorology, and drivers, *J. Geophys. Res. Atmospheres*, 2016JD025557, doi:10.1002/2016JD025557.

Woodcock, A. H. (1952), Atmospheric salt particles and raindrops, *J. Meteorol.*, *9*(3), 200–212, doi:10.1175/1520-0469(1952)009<0200:ASPAR>2.0.CO;2.

Xia, L., and Y. Gao (2010), Chemical composition and size distributions of coastal aerosols observed on the US East Coast, *Mar. Chem.*, *119*(1–4), 77–90, doi:10.1016/j.marchem.2010.01.002.

Yu, S., P. V. Bhave, R. L. Dennis, and R. Mathur (2007), Seasonal and Regional Variations of Primary and Secondary Organic Aerosols over the Continental United States: Semi-Empirical Estimates and Model Evaluation, *Environ. Sci. Technol.*, *41*(13), 4690–4697, doi:10.1021/es061535g.

Zhou, J., E. Swietlicki, O. H. Berg, P. P. Aalto, K. Hämeri, E. D. Nilsson, and C. Leck (2001), Hygroscopic properties of aerosol particles over the central Arctic Ocean during summer, *J. Geophys. Res. Atmospheres*, *106*(D23), 32111–32123, doi:10.1029/2000JD900426.

APPENDICES

Appendix A

A.1 Validation of Dry Diameters

Dry-dry scans were performed at the beginning, middle, and end of the deployment (26 April, 9 May, and 13 May, respectively. Figure A.1 shows the results of these scans. The beginning and end calibrations were performed for all three diameters (96, 188, and 284 nm). The middle calibration was only performed for the 98 nm dry diameter. Table A.1 shows the percent difference in the set dry diameter and the measured diameter. The percent difference for the three dry diameters was below 5%.

A.2 Simulations of the Particle Classification Method

Simulations were performed, similar to those by *Royalty et al.*, [submitted] to characterize the under and/or over prediction of the concentrations using the assumptions associated with the particle classification method. The simulations used prescribed variable number concentrations and chemical compositions for three different classes of aerosols. The simulation results summarized in Table A.2 show the uncertainties associated with a variety of different situations. Simulations shown in Table A.2 include: the assumption that the sulfate-like particle class is composed of ammonium sulfate, the assumption that the sulfate-like class was composed of ammonium bisulfate (ABS), and the varying of organic fractions.

Table A.1 The percent difference (%) in the set measured dry diameters (nm).

Set Dry Diameter (nm)	**Measured Dry Diameter (nm)**	**Percent Difference (%)**
98	96	2.91
196	188	4.05
292	284	2.01

Table A.2 Uncertainty simulations for the particle classification method.

Class	Simulation	Maximum Uncertainty (%)	Assumed Uncertainty (%)	
			Underestimation	Overestimation
Sodium-containing	ABS & Sodium Sulfate	-50	-65	50
	AS & Sodium Sulfate	-65		
	ABS & Artificial Seawater	50		
	AS & Artificial Seawater	-10		
Sodium-containing w/ organics	ABS & Artificial Seawater with Organics	-100	-100	--
	AS & Artificial Seawater with Organics	-100		
Carbon-containing	ABS with $\kappa = 0$	-40	-80	--
	AS with $\kappa = 0$	-7		
	ABS with $\kappa = 0.2$	-80		
	AS with $\kappa = 0.2$	-50		

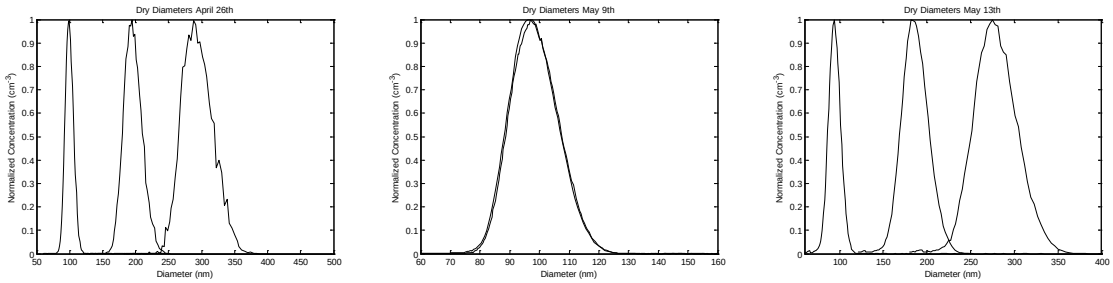

Figure A.1 Distributions for the dry-dry scans, a) at the beginning on 26 April, b) in the middle on 9 May, and c) at the end on 13 May.